Urban Climate 51 (2023) 101624

Contents lists available at ScienceDirect

Urban Climate

journal homepage: www.elsevier.com/locate/uclim

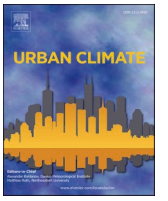

Spatial neighborhood analysis linking urban morphology and green infrastructure to atmospheric conditions in Karlsruhe, Germany

Marcel Gangwisch [a,b,*], Somidh Saha [c,d], Andreas Matzarakis [a,b]

[a] Research Centre Human Biometeorology, German Meteorological Service, Stefan-Meier-Str. 4, D-79104 Freiburg, Germany
[b] Chair of Environmental Meteorology, Institute of Earth and Environmental Sciences, Faculty of Environment and Natural Resources, University of Freiburg, Werthmannstr. 10, D-79085 Freiburg, Germany
[c] Institute for Technology Assessment and Systems Analysis (ITAS), Karlsruhe Institute of Technology, Karlstr. 11, D-76133 Karlsruhe, Germany
[d] Institute for Geography and Geoecology (IfGG), Karlsruhe Institute of Technology, Kaiserstr. 11, D-76133 Karlsruhe, Germany

ARTICLE INFO

Keywords:
Urban Heat Island
Normalized air temperature
Urban trees and forest
Bioclimate
Human thermal comfort

ABSTRACT

Urban areas are affected by the urban heat island effect, resulting in increased heat strain compared to rural areas. In this article, we aimed to study how urban morphology (e.g., building structure, sealing, and availability of green space) influenced meteorological variables and human thermal comfort on the microscale. Mobile measurements were performed during autochthonal weather conditions in Karlsruhe. Post-processing includes the transfer from a temporal (1 observation per s) to a spatial resolution (1 observation per 5 m), the normalization of the air temperature to the data range [0,1], and the spatial aggregation to account for inaccuracies in the Global Navigation Satellite System. The processed data were linked to the neighborhood's characteristics for a spatial analysis, specified by remotely-sensed and administrative geodata. The analysis encompassed the relationship of land use, sealing factor, and normalized difference vegetation index to the normalized air temperature. It revealed the dependency of the cooling effect of urban vegetation on the size as well as on the greenness of green spaces, while sealing showed an inverse effect. Our results will help urban planners take action during heat waves in the future. Furthermore, normalization enables the comparability of urban climate studies of varying latitudes and climate regions.

1. Introduction

Urban environments determined by climatic effects from the prevailing mesoscale down to the microscale influence the quality of life in cities. This refers mainly to the microscale's urban bioclimate, air quality, traffic, and noise in street canyons (Gehl, 2010; Matzarakis, 2020; Węziak-Białowolska, 2016). Therefore, bioclimate, and thus human thermal comfort, are severely threatened by the urban heat island effect (UHI), global climate change, increasing heatwaves, further sealing, and re-densification of urban areas (Masson et al., 2020a; Nowak and Greenfield, 2020; Revi et al., 2014; Santamouris, 2020).

A majority of studies focus on quantifying the UHI effect based on land surface temperature (LST) derived from satellite imageries.

* Corresponding author at: Research Centre Human Biometeorology, German Meteorological Service, Stefan-Meier-Str. 4, D-79104 Freiburg, Germany.
E-mail address: Marcel.Gangwisch@dwd.de (M. Gangwisch).

https://doi.org/10.1016/j.uclim.2023.101624
Received 3 January 2023; Received in revised form 24 April 2023; Accepted 22 July 2023
Available online 29 July 2023

However, these methods are currently insufficient for human-biometeorological purposes because the spatial resolution of freely available satellite imagery is insufficient for microscale analysis of urban areas (e.g., 30 m resolution of Landsat 7, and 8 and 20 m resolution of Sentinel-2 for the assessment of thermal infrared) (Ermida et al., 2020; Masson et al., 2020b; Sobrino et al., 2012). The temporal resolution is restricted to the overpass time of the space-borne platform, and the obstruction of the surface by clouds; i.e., a full assessment of diurnal cycles of the surface urban heat island (S-UHI) is currently not possible (Sobrino et al., 2012).

Furthermore, in the complex urban environment, remote sensing instruments cannot entirely capture energy conversions on vertical surfaces or facades due to effective anisotropy (Voogt and Oke, 1998). It is not possible to measure air temperature or humidity directly by space-borne remote sensing, only land surface temperature which results in S-UHI in urban environments (Voogt and Oke, 2003). Nevertheless, the complexity of the human thermal bioclimate cannot be reduced to the assessment of surface temperature; it is necessary to assess all atmospheric conditions (air temperature, relative humidity or vapor pressure, wind speed, and long- and shortwave radiation fluxes in terms of Mean Radiant Temperature) in urban environments (Parsons, 2014; VDI, 2021). These conditions can be summarized by thermal indices in a comprehensive way (Höppe, 1999; Jendritzky et al., 2012; Matzarakis et al., 1999; Staiger et al., 2019).

In contrast to remotely-sensed measurements, in-situ observations, spatial surveys and traverses were used to determine the characteristics of the UHI, or rather the urban heat archipelago, based on measurements of the air temperature (Chandler, 1962; Kotharkar and Surawar, 2016; Liu et al., 2017; Romero Rodríguez et al., 2020a; Saaroni et al., 2000). Based on these measurements, spatial interpolation based on geostatistics (Inverse Distance weighting, b-spline, nearest neighbor, triangulated irregular network or kriging (Longley, 2005)) and statistical approaches of machine learning were used to determine the UHI with high spatial resolution over the entire area.

The combination of satellite data (LST by Sentinel-2) and in-situ measurements by statistical models has previously been applied (Shandas et al., 2019; Voelkel and Shandas, 2017). Air temperature observations from a citizen science-driven measurement campaign were used to predict the extremes of UHIs using machine-learning techniques (RandomForest). The selected algorithm was applied with descriptors for land use and land cover (LULC), derived from survey images.

In order to quantify and map the urban microclimate spatially, data on the urban morphology in terms of land use, building morphology, and vegetation are necessary (Masson et al., 2020b). These data can be supplemented by demographic and traffic data to assess anthropogenic heat release to capture the leading causes of the UHI effect (Romero Rodríguez et al., 2020a). These variables must be related to in-situ observations, spatial surveys, traverses, and remotely-sensed datasets. (Romero Rodríguez et al., 2020a) describe the traversed environment with a discrete grid. The above parameters characterize each grid cell.

The urban morphological surroundings are a subset of the urban morphology in the proximity of a point of interest. The urban morphology represents the size, shape, and physical structure of a city and can be viewed from different perspectives with different focus (D'Acci, 2019).

Considering the urban morphology through remotely-sensed land-use classification (e.g. Local Climate Zones (LCZ, Stewart, 2011; Stewart and Oke, 2012), Urban Climate Zones (UCZ, Oke, 2004), CORINE Land Cover (CLC, Keil et al., 2005) or Urban Atlas 2018 (UA2018, European Union, 2018)) describes urban areas with varying degree of detail:

LCZ has been widely applied to assess the UHI effects as the temperature difference between different LCZ classes (Leconte et al., 2015; Lehnert et al., 2021). LCZ provides 17 different classes to characterize urban areas at a local scale (1×10^2 m - 1×10^4 m). LCZs are available for all of Europe at a spatial resolution of 100 m (Demuzere et al., 2019). However, the analysis based on LCZs is not suitable for the microscale due to insufficient detail in classes of urban areas, so the inner-zonal variation of the meteorological conditions cannot be resolved (Lehnert et al., 2015).

Vectorial Urban Atlas 2018 summarizes the distribution of urban, industrial, and green areas in a city and is especially suitable for European cities. Each type of land use is characterized by a different degree of building development, sealing, and greening, resulting in different thermal environments. Different resulting meteorological conditions characterize each environment in turn because it depends on the energy balance of the immediate surroundings, i.e., thermal properties (e.g., heat storage capacities), radiation-related properties (e.g., albedo and emissivity), and thus the sensible, latent, and radiative heat fluxes in the proximity (ASHRAE, 2017; Oke et al., 2017). Furthermore, intrinsic processes modify the thermal environment. These include anthropogenic processes (e.g., combustion), and natural processes such as the microclimate regulation by transpiration and shading of urban trees (Ferrini, 2017; Jones, 2013; Monteith and Unsworth, 2013).

In order to evaluate the thermal effects on the microscale of individual urban trees and buildings in an open system (such as the urban environment), it is not sufficient to consider only land use, since these classes cannot represent the diversity (of buildings and trees), and especially cannot resolve vertical structures.

Urban tree cover and species identity can significantly influence the urban microclimate at cityscape level. For instance, (Morakinyo et al., 2020) used ENVI-met simulators to use 54 generic tree forms and 10 urban morphology characteristics to prove that correct species selection is crucial to reduce the impact of UHIs. A study using Landsat imageries on 156 remotely-selected sample plots from 15 greenspaces in the city of Changzhou in China found that tree species diversity and tree canopy coverage can mitigate the heat stress created by UHIs (Wang et al., 2021). At single tree level, transpirational cooling can ameliorate urban microclimate at local level which can vary between species (Rahman et al., 2017, 2020).

However, upscaling and modeling studies on the interrelationships between tree cover and urban microclimate by combining remotely-sensed data with field measurements from replicated sampling units covering diverse urban morphology are rare in the literature.

In this article, we quantified the microscale effects of urban morphological surroundings on the atmospheric conditions, and thus also on the bioclimate, based on remotely-sensed data, in-situ observations, and administrative data (e.g., managed tree cadaster and

real estate cadaster) for the municipality of Karlsruhe in Germany. Mobile measurements were generalized to determine air temperature and humidity anomalies, along with a spatial survey without the influence of the absolute measured values. The measurement data were extensively processed to extinguish errors in the accuracy of the Global Navigation Satellite Systems (GNSS) in the city, and systematic errors (e.g., at traffic lights). The processed data were used to reveal relationships between observed meteorological conditions and urban structures near the route of mobile measurements. Vicinity to the route was characterized as a neighborhood by representative parameters: shares of Urban Atlas classes, Sealing and Normalized Difference Vegetation Index (NDVI). The size of the circular neighborhood was varied, and studied between 5 m to 500 m of the route, since the thermal range of individual urban structures (in terms of heat transfer) is unknown and dependent on the respective wind direction and -speed.

Based on the relation between normalized air temperature and characterized neighborhood the following research questions are addressed:

1. How can spatial measurement runs be used to quantify urban heat island effects?
2. What is the thermal influence of urban green and gray infrastructure on the ambient air temperature?
3. How can local observation, remote sensing, and administrative data be combined and applied for short- and long-term climate adaptation and mitigation?

Urban planners and architects can actively modify all representative variables of a neighborhood to improve the quality of life for people in cities, but knowledge about the thermal effects of urban structures is crucial to do so, and enable reaction to the effects of a typified heat wave (Gehl, 2010).

2. Material and methods

2.1. Study area in Karlsruhe, Germany

Karlsruhe is located in the warm Upper Rhine Valley in Germany. The city center is located at 49.0°N, and 8.4°E at about 115 m above mean sea level (Fig. 1). In 2021, 308,436 inhabitants lived in an area of 173.4 km^2 (≈ 1778 inhabitants per km^2) in Karlsruhe (Stadt Karlsruhe, 2021).

In 2003, Germany's air temperature record of 40.2 °C, valid until 2015, was set at the meteorological station in Karlsruhe. The high heat stress in the Upper Rhine Valley reflects various climatic particularities, some of which are orographically caused. These result in warm, humid air, and high irradiation combined with low wind speeds (Hackenbruch, 2018), reflecting the Köppen-Geiger class Cfb for warm temperate; fully humid with warm summer (Rubel and Kottek, 2010).

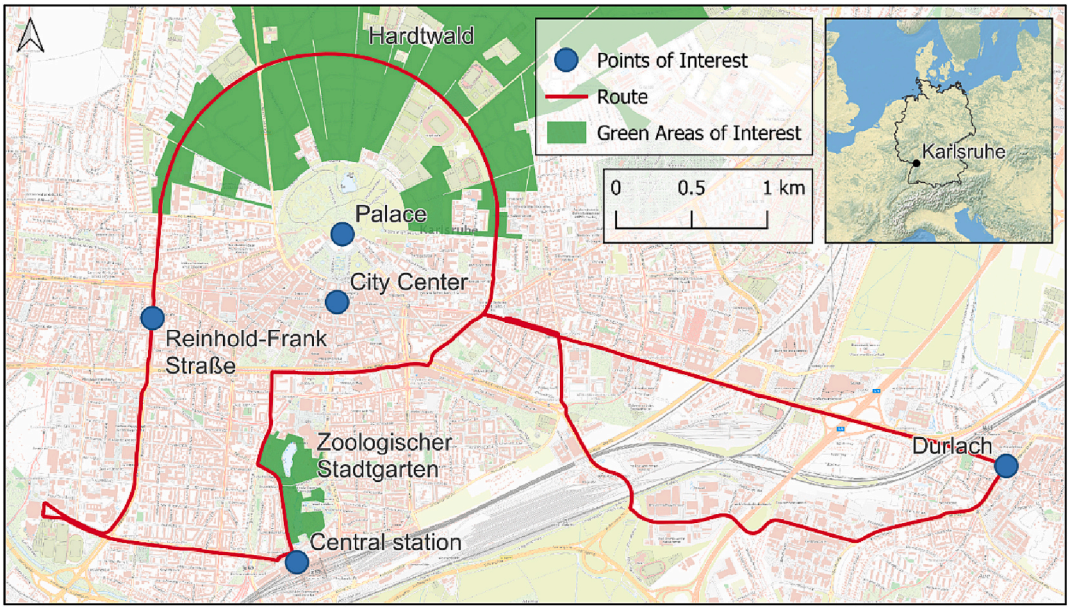

Fig. 1. Study area and mobile measurement route in Karlsruhe, Germany. Additional points and areas of interest are shown for discussion: Hardtwald is an urban forest in the north of the city center, Reinhold-Frank-Straße is a busy main road, Zoologischer Stadtgarten is an urban park, with green spaces and water bodies, Durlach is an urban district with a distinctive old town. The palace is the main landmark of Karlsruhe.
Main basemap: TopPlusOpen © Federal Agency for Cartography and Geodesy (2023),
Aside basemap: Made with Natural Earth. (For interpretation of the references to colour in this figure legend, the reader is referred to the web version of this article.)

2.2. Mobile measurements to determine the microscale influences of gray and green infrastructure

Spatial surveys were carried out with a mobile measurement vehicle in 2019 and 2020, each in June during the hot season in Karlsruhe (Fig. 2). The measurement vehicle drove through the most significant areas in Karlsruhe on a route with length of 19.6 km (which lasts 20 min on an average per run) (Fig. 1). The meteorological variables were measured with a temporal resolution of 1 observation $\cdot s^{-1}$. Therefore, the spatial resolution is variable due to the dynamic driving speed. Nevertheless, a constant speed of 30 km/h was maintained in urban areas as per the suggestion from (Ketterer and Matzarakis, 2015), and 50 km/h in rural areas, especially on highways in accordance with (Soltani and Sharifi, 2017).

The meteorological measurement system was installed at the front of the measurement vehicle and included measurements of actively ventilated air temperature (T_a, °C) and relative humidity (RH, %) at 0.7 m and 2.0 m AGL, as well as surface temperature (T_0, °C) and global radiation (G, W/m^2). Descriptive statistics of air temperature in the raw data are shown in Table 1 and Table 2. In total, the route was surveyed 26 times. In 2019 there were seven trips during the day and four during the night. In 2020 there were eight trips during the day and seven during the night. All measurement runs were carried out with a time interval of three hours.

The measurements were conducted during autochthonous weather conditions in order to determine the local and regional influences of urban structures, and vegetation. A barometric ridge gave the conditions for a successful measurement campaign over Central Europe in combination with a corresponding surface high. Large-scale subsidence prevented almost all cloud formation. The UHI condition was clearly pronounced during the measurement periods.

2.3. Preprocessing and preparation of observed data

The common challenges in mobile measurements are spatial and temporal accuracy (e.g., at traffic lights, traffic jams, GNSS inaccuracy) and human error (e.g., driving errors). Therefore, sequential preprocessing steps were implemented, and encompass the aggregation, relation, generalization, and transformation of the recorded data to counteract those errors (Fig. 3).

The preprocessing was conducted with R version 3.6.1, a free software environment for statistical computing suitable for human biometeorological analysis (Charalampopoulos, 2020; R Core Team, 2019). Further geoprocessing packages (rgdal-1.5-16, raster-3.3-13, exactextractr-0.4.0) and the Geographic Information Systems (GIS) Quantum GIS (QGIS-3.20.0 RC) and SAGA GIS (2.3.2) (Conrad et al., 2015) were utilized. We have described the steps which were followed during the preprocessing of the data:

1. Raw data was first provided in comma separated values format (CSV) for each measurement run and then further processed in the GeoPackage format (Yutzler, 2021);
2. All outliers with a value greater than three times the standard deviation were removed from the data sets. Then, the data points with a wind speed of $<0.5\, m \cdot s^{-1}$ or $>3.0\, m \cdot s^{-1}$ were filtered out. Wind speed was obtained from the nearest meteorological station;
3. All measurement runs were sorted into four groups according to the time of day. The first group includes all runs during the night (between 22 and 4 UTC). The second group sorted the runs in the morning (between 4 and 10 UTC), and the third group sorted the runs during midday (between 10 and 16 UTC). Finally, the last group contains the runs in the evening (between 16 and 22 UTC);

Fig. 2. Measurement vehicle of the German Meteorological Service to measure air temperature, relative humidity (at 0.7 m and 2.0 m height above ground level (AGL)), surface temperature and global radiation.

Table 1
Descriptive statistics for the observations of air temperature at 2.0 m AGL in Karlsruhe in June 2019.

Time [LST]	Time [UTC]	Min [°C]	Mean [°C]	Max [°C]
0–6	22–4	13.9	18.3	22.0
6–12	4–10	19.5	23.3	28.7
12–18	10–16	26.3	29.4	33.1
18–24	16–22	18.9	25.1	29.3

Table 2
Descriptive statistics for the observations of air temperature at 2.0 m AGL in Karlsruhe in June 2020.

Time [LST]	Time [UTC]	Min [°C]	Mean [°C]	Max [°C]
0–6	22–4	12.3	17.8	21.7
6–12	4–10	19.4	23.7	27.6
12–18	10–16	26.4	28.5	31.3
18–24	16–22	17.2	24.4	29.5

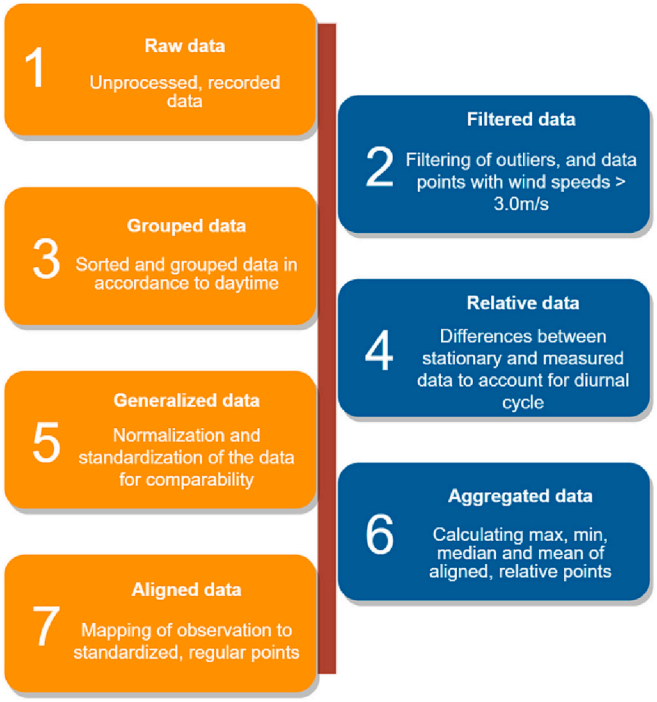

Fig. 3. The steps for preprocessing and preparation of recorded data for the Spatial Neighborhood Analysis.

4. The data were set to the closest measuring station (10-min data) (Eq. 1). All observed variables ($p_{obs} \in \{T_a, RH, VP, T_s, G\}$) of each measurement run were related to the closest official meteorological station in Karlsruhe in order to account for the diurnal cycle of the corresponding variable:

$$p_{rel} = p_{obs} - p_{station} \qquad [unit(p_{obs})] \tag{1}$$

5. The related observations (p_{rel}) are further differenced (Eq. 2), normalized (Eq. 3) and standardized (Eq. 4) to generalize from the absolute measured values:

$$p_{\Delta} = p_{rel} - mean(p_{rel}) \qquad [unit(p_{obs})] \tag{2}$$

$$p_{norm} = \frac{p_{rel} - min(p_{rel})}{max(p_{rel}) - min(p_{rel})} \qquad [0, 1] \tag{3}$$

$$p_{stand} = \frac{p_{rel} - mean(p_{rel})}{SD(p_{rel})} \qquad [unit(p_{rel})] \tag{4}$$

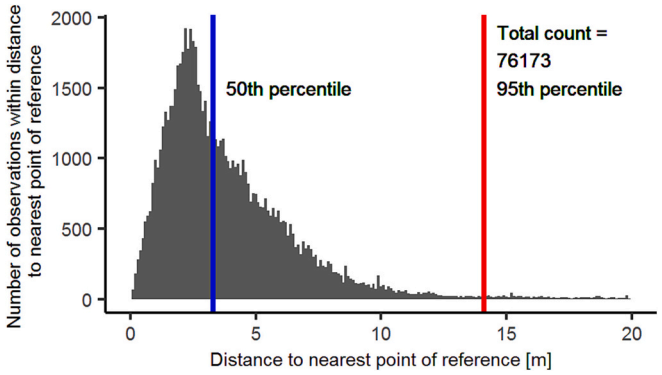

Fig. 4. Distribution of the distances between registered GNSS positions and standardized reference points.

The calculation of p_{Δ}, p_{norm} and p_{stand} ideally allows a direct comparison of the measurements independent of the time of day and year in which the measurements were recorded. p_{norm} was considered in the subsequent neighborhood analysis and applied to the relative, observed air temperature at 2.0 m AGL;

6. Due to the inaccuracy of GNSS, the measurement runs were several meters apart, although they were carried out on the same route (Fig. 5a). The mean error of all GNSS positions was 9.2 m, while 95% of all observations were within 14.1 m of the route (Fig. 4). An artificial data set with synthetic reference points with predefined positions, which was within exactly the driven route at a regular distance of 5 m, was created (Fig. 5b). The positions of these reference points were determined using the georeferenced roads from

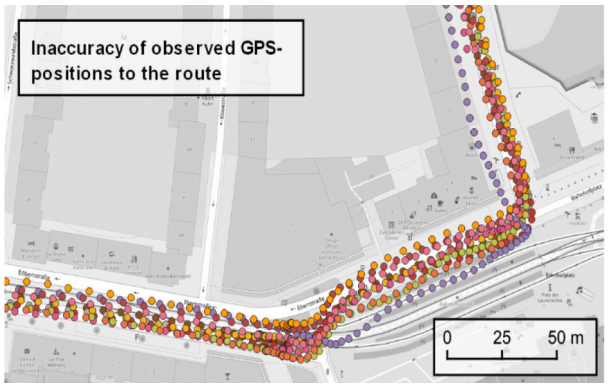

(a) Variance of measured locations based on GNSS positions of a selection of the route.

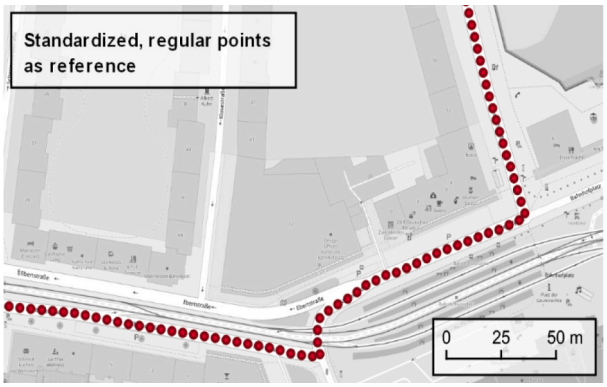

(b) Definition of fixed, standardized, regular points in space with the correct position as a reference.

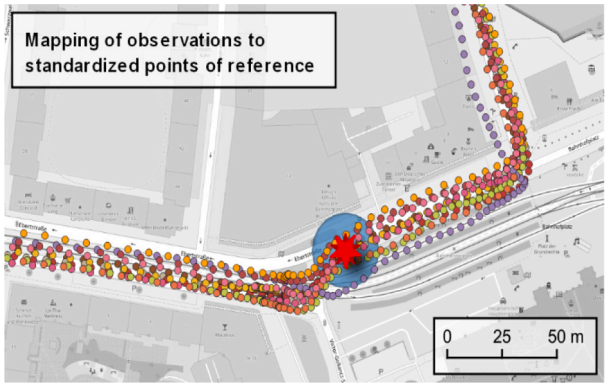

(c) Aggregation of measurements according to the standard error of GNSS positions along the route for each standardized reference point.

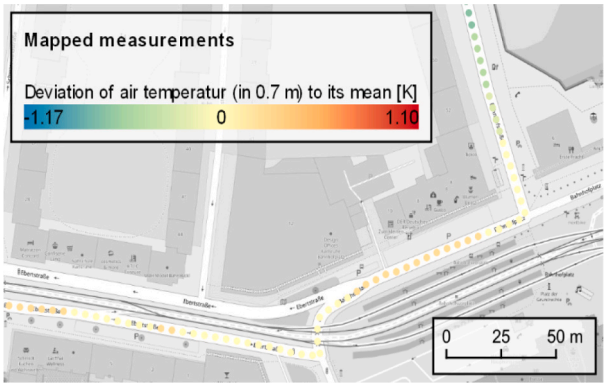

(d) Aggregated measurements along the route for each standardized reference point.

Fig. 5. Pipeline of preprocessing to align and aggregate mobile measured meteorological data. The procedure is exemplarily shown in detail only for a subsection of the route. (Basemap by OpenStreetMap).

the OpenStreetMap dataset. This new artificial data set was used to correct the inaccuracies of GNSS positions and align the measurement runs spatially. Each measurement run was spatially aligned, based on the reference points, so that the normalized parameters were mapped to the reference points;

7. Finally, for each reference point, the max/min/mean/median normalized condition within a radius of 15 m of the overlapping and aligned observations was calculated (Fig. 5c). The radius of 15 m was selected due to the 95th percentile in the recorded locations during measurements (Fig. 4). This method ensures that all measurement runs and points are then located at the same georeferenced position. In these ways, the observations were also transferred from a temporal (1 observation per second) to a spatial observation series (1 observation per 5 m), and clustered measuring points (e.g., at traffic lights) were averaged (Fig. 5d).

2.4. Representation of the urban morphology in the neighborhood of the route

In theory, the meteorological variables ($T_{a,0\ m}$, $T_{a,0.7\ m}$, $T_{a,2.0\ m}$, $RH_{0.7\ m}$, $RH_{2.0\ m}$, $VP_{0.7\ m}$ and $VP_{2.0\ m}$) depend on the energy balance of the immediate surroundings, and thus on sensible, latent, and radiative heat fluxes in the proximity to the route. These fluxes are influenced by different surface properties of the immediate surroundings (i.e., thermal properties (heat storage capacities and thermal conductivity), radiation-related properties (albedo and emissivity)) but also by intrinsic, anthropogenic, and natural processes in the city. These include, for example, combustion processes as well as tree-physiological processes (e.g., transpiration and photosynthesis). In addition, the outgoing and incoming radiation fluxes are determined by the Sky View Factor (SVF), which in turn is significantly influenced by the height of surrounding buildings and spacing between buildings.

The classification according to Urban Atlas 2018, was first used to quantify the spatial influence of immediate surroundings. This classification differentiates between five urban development classes based on the prevailing degree of sealing (section 2.4.1).

The immediate surroundings were additionally examined separately for the gray and green infrastructure. We undertook the following steps for that purpose:

1. The structure in a neighborhood was quantified by imperviousness (e.g., roads, buildings, and infrastructure) (European Union, 2018) (section 2.4.2);
2. The vegetation was taken into account by remotely-sensed Normalized Difference Vegetation Index (NDVI) (Ermida et al., 2020). In addition, data from the tree cadaster of the municipal garden and civil engineering departments were used (section 2.4.3).

The open-source GIS systems SAGA GIS (2.3.2) (Conrad et al., 2015) and QGIS (3.20.0 RC) (Open Source Geospatial Foundation, 2018) were used to prepare the descriptors for subsequent neighborhood analysis. First, all descriptors were resampled to the spatial resolution of 1 m and transformed to the same metric projection (WGS 84 / UTM zone 32 N - SRID:32632), suitable for the study area.

2.4.1. Representation of the land use according to urban atlas 2018 land-use classification in the neighborhood (European Union, 2018)

Urban Atlas 2018 is a high-resolution (20 m) remotely-sensed dataset (European Union, 2018). A land-use classification based on 27 classes classifies urban areas based on urban fabrics, industrial areas, transportation infrastructure, artificial non-agricultural areas, and natural/semi-natural areas (Table 3). The Urban Atlas 2018 dataset is available in a vector data format compliant with standards of the Open Geospatial Consortium (OGC).

The measurement route is characterized according to the Urban Atlas classification in the neighborhood (Fig. 6a). For this purpose, the proportions of each land-use type within a radius of 5 m to 500 m from each preprocessed measuring point were recorded. The proportion of Urban Atlas classes UA2018:11100, UA2018:11210, UA2018:11220, among others, were calculated and assigned to

Table 3
Urban Atlas 2018 land-use classification dividing the land into 17 urban classes and 10 rural classes for land use and land cover (European Union, 2018). Each class evokes a specific thermal environment.

Code	Nomenclature	Code	Nomenclature
Urban Fabric		13100	Mineral extraction and dump sites
11100	Continuous urban fabric (S.L. > 80%)	13300	Construction sites
11210	Discontinuous dense urban fabric (S.L. 50% - 80%)	13400	Land without current use
11220	Discontinuous medium dense urban fabric (S.L. 30% -50%)	Artificial non-agricultural vegetated areas	
11230	Discontinuous low-density urban fabric (S.L. 10%-30%)	14100	Green urban areas
11240	Discontinuous, very low-density urban fabric (S.L. < 10%)	14200	Sport and leisure facilities
11300	Isolated Structures	Agricultural areas	
Industrial areas		21000	Arable land (annual crops)
12100	Industrial, commercial, public, military and private units	22000	Permanent crops
Transportation Infrastructure		23000	Pastures
12210	Fast transit roads and associated land	24000	Complex and mixed cultivation
12220	Other roads and associated land	25000	Orchards
12230	Railways and associated land	Natural and semi-natural areas	
12300	Port areas	31000	Forests
12400	Airports	32000	Herbaceous vegetation associations
		33000	Open spaces with little or no vegetation
		40000	Wetlands
		50000	Water

each observation. The frequencies of the land-use types in different neighborhoods to the measurement route (5 m to 200 m) is shown in the histogram and corresponds essentially to that of the entire city (Fig. 6b). Densely built-up, urban-, industrial-, and wooded areas represent the central part of land use in the city. Thus, it is assumed that the survey route represented the entire city.

2.4.2. Representation of the gray infrastructure in the neighborhood

(European Union, 2018) also provides a high-resolution layer (HRL) for the degree of sealing. The layer for imperviousness is a remotely-sensed dataset in 20 m spatial resolution, which depicts the dimensionless degree of sealing from 0 to 1. Areas with a sealing degree of 0 (e.g., urban forests) are undeveloped, unsealed areas. These surfaces are characterized by a reduced heat storage capacity and increased evapotranspiration.

In contrast, wholly sealed areas have a sealing degree of 1 (e.g. inner-city areas). These areas are characterized by an increased heat storage capacity and reduced evapotranspiration. The imperviousness within a radius of 5 m to 500 m from each measuring point was recorded and is exemplarily shown in Fig. 7.

2.4.3. Representation of green infrastructure in the neighborhood

Vegetation in the proximity to the route was parameterized by the Normalized Difference Vegetation Index (NDVI), because this dataset is available for the entire urban area, especially for the urban forest in the north (*Hardtwald*) (Fig. 8). NDVI was calculated from remote satellite imagery of Landsat-8. Landsat-8 provides thermal infrared spectral bands (TIR) through its sensors TM, ETM+, and TIRS, to calculate NDVI in a resampled resolution of 30 m. NDVI was calculated by the script of (Ermida et al., 2020), utilizing Google Earth Engine and the spectral bands for near-infrared (NIR) and red (R) of Landsat-8. The index is defined as:

$$NDVI = \frac{NIR - R}{NIR + R} \qquad [0, 1] \tag{5}$$

NDVI is 0 if the respective surface is fully sealed and not covered with vegetation, and 1 in fully vegetated and unsealed areas.

NDVI is available throughout the whole city but does not provide further information about the obstruction of the upper hemisphere. This means that shading effects due to the tree canopy cannot directly described by NDVI. Depending on the density of the tree

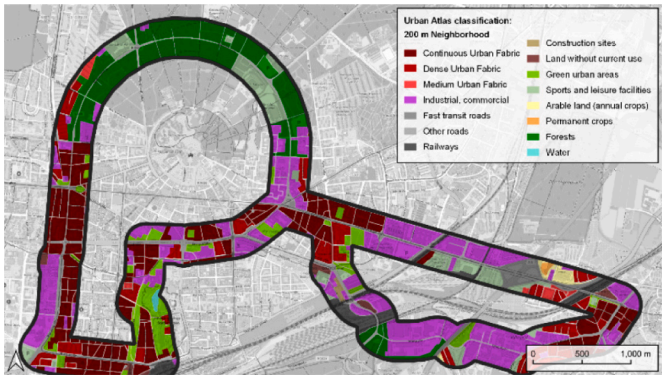

(a) Spatially resolved urban atlas classes in 200 m range of the measurement route. (Basemap by OpenStreetMap)

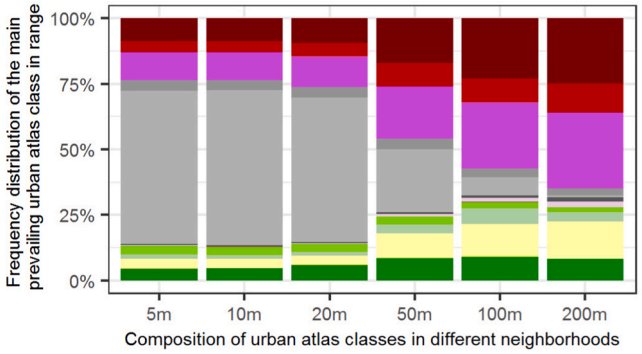

(b) Variation of the prevailing land-use classification concerning the considered neighborhood.

Fig. 6. Characteristics of the neighborhood in terms of land-use types. For detailed description of the LULC classes see Table 3.

Fig. 7. Representation of the gray infrastructure in the 200 m neighborhood to the route by remotely-sensed imperviousness (European Union, 2018). This layer contains the sealing in the entire urban area in 20 m spatial resolution. (Basemap by OpenStreetMap).

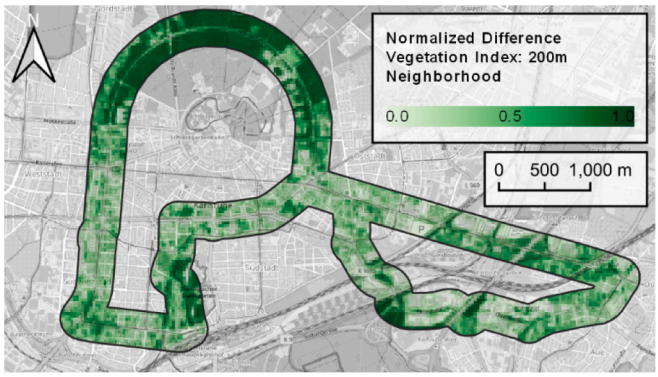

Fig. 8. Representation of green infrastructure in the neighborhood in 200 m range to the route. Remotely-sensed Normalized Difference Vegetation Index based on the script by (Ermida et al., 2020) with 30 m spatial resolution. (Basemap by OpenStreetMap). (For interpretation of the references to colour in this figure legend, the reader is referred to the web version of this article.)

canopy, longwave radiation emitted by surfaces below the tree canopy could also be limited and not assessed by NDVI.

2.5. Spatial neighborhood analysis

All descriptors mentioned above were used to characterize the immediate vicinity of the measurement route. In addition, for each measuring point, descriptors values within a radius of 5 m to 500 m were used. The preprocessed meteorological data (Fig. 3) were

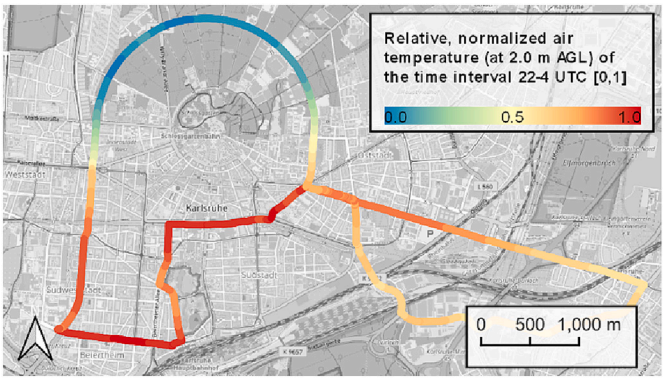

Fig. 9. The night conditions (22–4 UTC) showed the urban heat island effect in its most dominant form. The difference in air temperature between urban and rural areas (from Karlsruhe city center to Karlsruhe Durlach) was clearly pronounced and the cooling effect of the adjacent forest (*Hardtwald* (LCZ B)) in the north was most prominent.

related to the characteristic descriptors of the neighborhood to show the effects of urban structures and vegetation on the urban atmospheric conditions.

3. Results

In the following, we first show the results of the preprocessing of the measurement data from steps 1 to 7 (Fig. 3). Subsequently, the results of the actual spatial neighborhood analysis are presented for imperviousness and NDVI along the route.

3.1. Relative and normalized mobile measurements

The relative and normalized air temperature at 2.0 m AGL was clearly dependent on the time of day, thus the results are depicted in Fig. 9 to Fig. 13 for the respective time intervals (22–4, 4–10, 10–16, and 16–22 UTC) as described in Fig. 3. Fig. 9 to Fig. 13 shows the development of the urban heat archipelago along a partial measurement route in Karlsruhe, Germany for four time intervals. The relative and normalized air temperature at 2.0 m AGL showed the cooling effect of adjacent urban forests and parks, but also hotspots of unobstructed streets and open spaces.

The night condition (22–4 UTC) depicted the UHI in its most dominant form. The spread of the air temperature as expressed as the difference between absolute minimum and maximum was the largest value with 5.6 K compared to other time intervals (Table 4). This spread represented the classic UHI intensity in Karlsruhe, assessed by measured air temperature.

This was particularly evident from the relative and normalized air temperature difference between the core of the city, south of *Karlsruhe Palace* (LCZ 6) and *Karlsruhe Hardtwald* (LCZ B) in the north (Fig. 9). In addition, a decreasing gradient of relative and normalized air temperature between *Karlsruhe city center* (LCZ 2) and *Karlsruhe Durlach* (LCZ 5) in the east was pronounced. Overall, the relative and normalized air temperature during the nighttime condition was relatively homogeneously distributed throughout the study area and thus characterized by large spatial auto-correlation. The normalized air temperature was not changing in an abrupt manner. The most significant changes took place in areas of land use change (e.g., at forest boundaries).

Spatial auto-correlation was analyzed separately in a variogram for the four time intervals (Fig. 10). In the variogram it can be clearly seen that the variance of relative and normalized air temperature at 2.0 m AGL with increasing distance between the measuring points was lower in the night condition (in blue) than during the day (in red). This means that the small-scale influence of different urban structures within the city was minimal during the night.

The condition in the morning (4–10 UTC) showed the weakening of the UHI effect - the spread was reduced to 3.3 K. At the same time, the cooling by urban trees intensified with increasing solar irradiance and Photosynthetically Active Radiation (PAR) in the *Hardtwald* area (LCZ B), but especially in the *Zoologischer Stadtgarten* (LCZ 6 and B) (Fig. 11). The observed values of air temperature at 2.0 m AGL were spatially heterogeneous and exhibit more significant variance than at night (Fig. 10).

The conditions at noon (10–16 UTC) showed a further intensification of the cooling effect of urban parks. Especially *Zoologischer Stadtgarten* (LCZ 6 and B) in the south unfolded its cooling potential (Fig. 12). At the same time, measurement results showed a greater variation. This also decreased spatial autocorrelation, which was reflected in an increase in the variance of relative and normalized air temperature (Fig. 10). The warmest area along the measured section was on the busy main road (*Reinhold-Frank-Straße*).

The evening conditions (16–22 UTC) showed the spatial development of the UHI (Fig. 13). The spread was increasing again to 5.2 K. The same pattern as in the night but with a lower magnitude was recognizable, meaning that the UHI was not yet fully developed (compare Fig. 9 and Fig. 13).

3.2. Influence from different neighborhoods

For each observation, each descriptor in the 5 m to 500 m orbit to the route was calculated. Descriptors for gray infrastructure (imperviousness (Fig. 7)) and green infrastructure (NDVI (Fig. 8)) were applied and related to the derived relative and normalized air temperature at 2.0 m AGL. The complete result set for all time intervals and buffer sizes is given in Appendix A and B. In the following, only selected buffer sizes and time intervals are presented for simplicity. It is important to note that the number of observations per descriptor class did not vary between different time intervals, but between the analyzed buffers by design of the analysis.

3.2.1. Impact of gray infrastructure

High degree of sealing in urban areas (bars in dark-red) resulted in high values of relative and normalized air temperature at 2.0 m

Table 4
Descriptive statistics (min, max, standard deviation) of the processed air temperature at 2.0 m AGL. The data of each interval was related to the nearest meteorological station. Local Climate Zones of minima and maxima locations are given to classify and compare the results to other studies. The spread (difference between min and max) corresponds to the urban heat island intensity.

Time [UTC]	Min [K]	LCZ_min	Max [K]	LCZ_max	SD [K]	Spread [K]
22–4	−3.8	B	1.8	6	1.3	5.6
4–10	−1.4	8	1.9	6	0.6	3.3
10–16	−1.5	5	1.6	6	0.5	3.1
16–22	−3.2	A	2.0	6	1.0	5.2

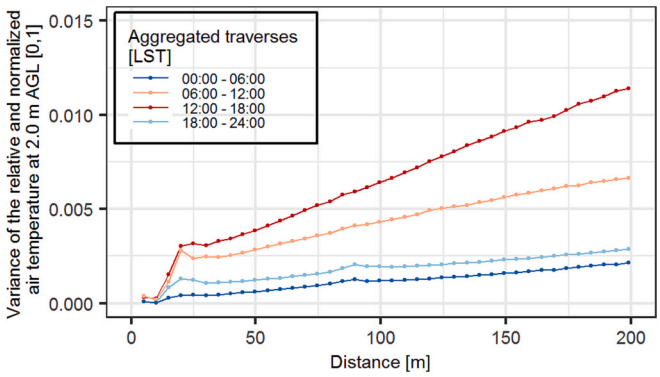

Fig. 10. Variogram showing the spatial autocorrelation of relative and normalized air temperature at 2.0 m AGL.

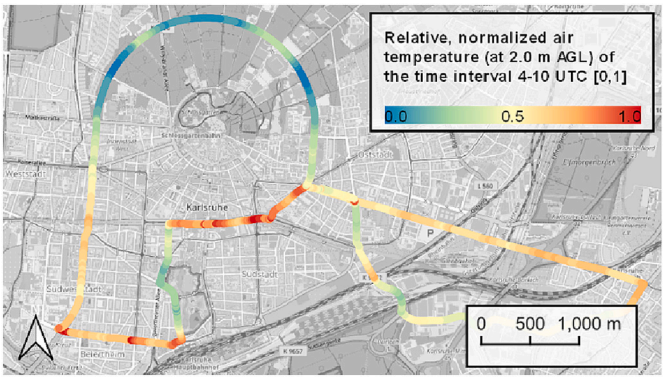

Fig. 11. The conditions in the morning (4–10 UTC) showed the weakening of the UHI due to morning insolation. The transpirational cooling effect of urban parks and the heating of open squares and streets started.

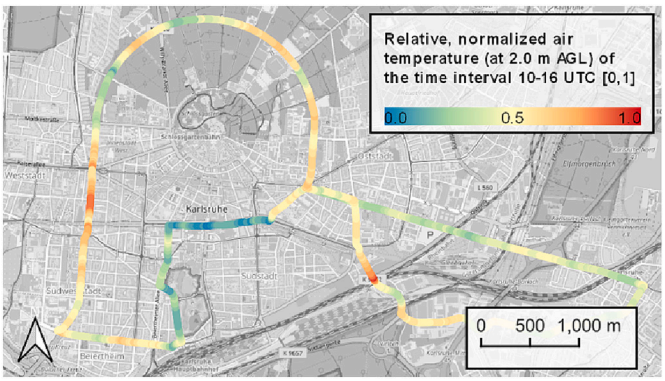

Fig. 12. The conditions at noon (10–16 UTC) showed further intensification of the cooling effect of urban parks. Especially the *Zoologischer Stadtgarten* (LCZ 6 and B) in the south unfolded its cooling potential. At the same time, measurement results showed a greater variation due to thermally induced mixing by convection and advection.

AGL, especially during the nighttime intervals 22–4 UTC and 16–22 UTC, independently of the buffer size (Appendix A). The median values were increasing from left to right for each of these time intervals. The nocturnal intervals were, independently of the buffer size, above the levels of diurnal intervals and thus represent the nocturnal intensity of UHI on the normalized scale between 0 and 1.

We present the results for sealing within 100 m range in the morning hours (22–4 UTC) in detail (Fig. 14). Areas with low degree of sealing (white) were cooler in terms of relative and normalized air temperature at 2.0 m AGL ($median(T_{a,2.0,norm}) \approx 0.6$) compared to areas with high degree of sealing (dark-red) ($median(T_{a,2.0,norm}) \approx 0.8$).

Unsealed areas (gray) were the coldest of the study areas ($median(T_{a,2.0,norm}) \approx 0.1$), but showed the greatest interquartile range

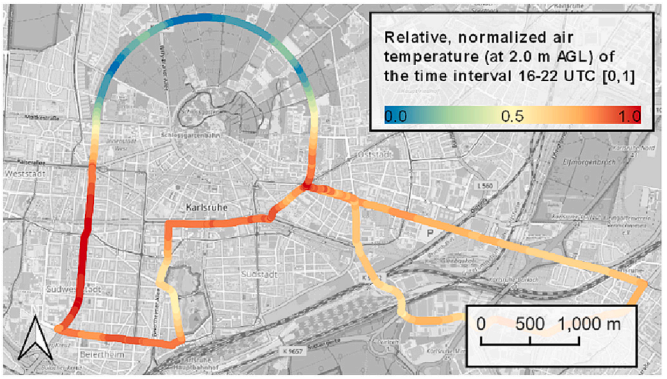

Fig. 13. The evening conditions (16–22 UTC) showed the spatial development of the urban heat island. The same structure as in the night (Fig. 9) but with a lower magnitude was recognizable.

(IQR). This increase of relative and normalized air temperature from low- to high degree of sealing was also observable in the morning (4–10 UTC) and evening (16–22 UTC) hours throughout all buffer sizes.

The conditions after noon (10–16 UTC) showed an indifferent pattern without a clear structure. The relative and normalized air temperature remained rather constant ($T_{a,2.0,norm} \approx 0.5$) (Appendix A).

The size of the buffer, and therefore the size of the unsealed area in range, was most important for cooling. The cooling effect was increased with an increased size of the unsealed area. Large-scale unsealed areas in a 500 m range to the route had therefore the most significant impact on cooling. In the morning condition (22–4 UTC), the median value for normalized and relative air temperature at 2.0 m AGL dropped from ≈ 0.5 to 0.1 for buffer sizes from 5 m to 500 m (Fig. 15).

It was found that cooling by small unsealed (and possibly vegetated) surfaces was more effective during the day in comparison to the night. With the increasing size of the unsealed area (radius larger than 50 m) the relative and normalized air temperature decreased faster at night, so that large and unsealed areas were also coolest at night and the aforementioned observation was inverted.

3.2.2. Impact of green infrastructure

Green infrastructure, expressed by the Normalized Difference Vegetation Index, showed an inverse impact on the urban thermal

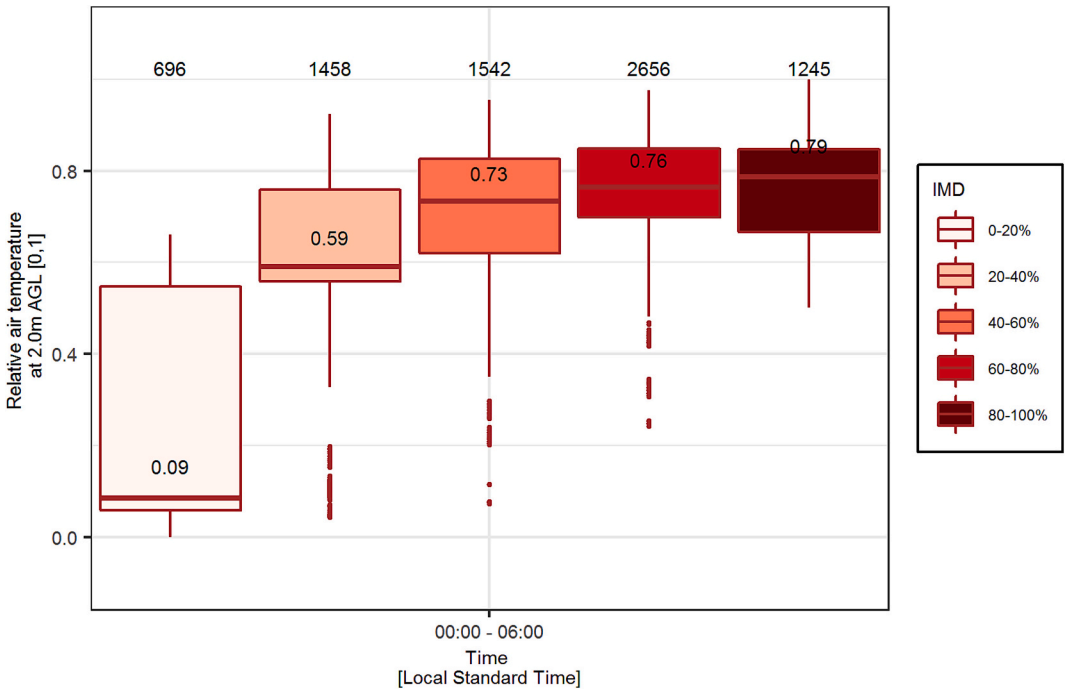

Fig. 14. Modification of relative and normalized air temperature at 2.0 m AGL in morning hours (22–4 UTC) by sealing within 100 m range by its magnitude. The degree of sealing is divided into groups with intervals of 20%, increasing from left to right. Remotely-sensed imperviousness was provided by (European Union, 2018).

environment. High degree of greening led to low values of relative and normalized air temperature at 2.0 m AGL independently of the buffer size under consideration (Appendix B). This holds for each time interval except for the daytime interval (10–16 UTC), when the relative and normalized air temperature remained rather constant.

We present the results for NDVI within 100 m range in the morning hours (22–4 UTC) in detail (Fig. 16a). Areas with low degree of NDVI (light-green) were warmer ($median(T_{a,2.0,norm}) \approx 0.8$) compared to areas with high degree of NDVI ($median(T_{a,2.0,norm}) \approx 0.1$). A more detailed analysis revealed that the warmest areas were located in densely built-up urban (dark-red) and industrial areas (pink), according to the Urban Atlas classification. The coldest zones were clearly located in the urban forests (green) (Fig. 16b).

The dependency on the size of the area under consideration is also evident for NDVI, just as it is for sealing (Fig. 17). With an increase in the greened area from 5 m to 500 m, the mean relative and normalized air temperature decreases from ≈ 0.6 to 0.1 for NDVI-levels between 60% to 100%.

When we look at Fig. 6, Fig. 15 and Fig. 17, we notice that the change in land use and the change in relative air temperature by unsealed and vegetated areas show a similar pattern as the buffer size increases.

4. Discussion

The observed intensity of the urban heat island in Karlsruhe is comparable to results of over 100 cities in Australia and Asia. The average UHI intensity as observed by studies in Australia and Asia using mobile traverses was 4.1 K (Santamouris, 2015). The average observed spread in Karlsruhe was 4.3 K with fluctuations between 3.1 K and 5.6 K, and therefore comparable to mentioned UHI intensities (Table 4). The greatest intensity of the UHI (the largest spread) was also observed in the nighttime period between 22 and 4 UTC (Table 4), as also shown by other studies (Arnfield, 2003; Dobrovolný and Krahula, 2015).

4.1. Relative and normalized air temperature

In this study, measurements were referenced to the nearest meteorological station and then min-max-normalized to the unit-less range between 0 and 1 (Eq. 1–3). The proposed method is in principle independent of the geographic location and of the prevailing weather conditions due to the abstraction of absolute values. We decided on a specific, representative weather condition that represents the conditions during a heat wave, while all measurements were related to the nearest two meteorological stations.

For comparability of different cities of mid-latitude, we propose a meteorological framework. Wind speed should be above 0.5 $m \cdot s^{-1}$, below 3.0 $m \cdot s^{-1}$, and the daily maximum air temperature should be above 30 °C with clear sky conditions. Standardization of these meteorological boundary conditions lead to a transferable method, which can be applied to other cities in such a way that the results, which describe the UHI, are also comparable.

The distribution of the data is not altered by min-max normalization but it is not directly possible to revert the dimensionless values to the original UHI intensities unless the minimum and maximum values of the respective cold and hot spots are explicitly measured. If

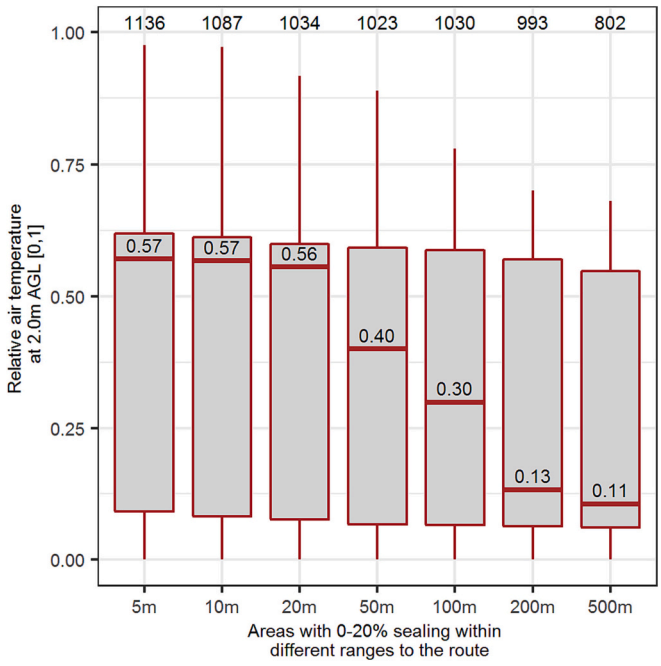

Fig. 15. Modification of relative and normalized air temperature at 2.0 m AGL in morning hours (22–4 UTC) by the area size under consideration with sealing between 0% -20%. Remotely-sensed imperviousness was provided by (European Union, 2018).

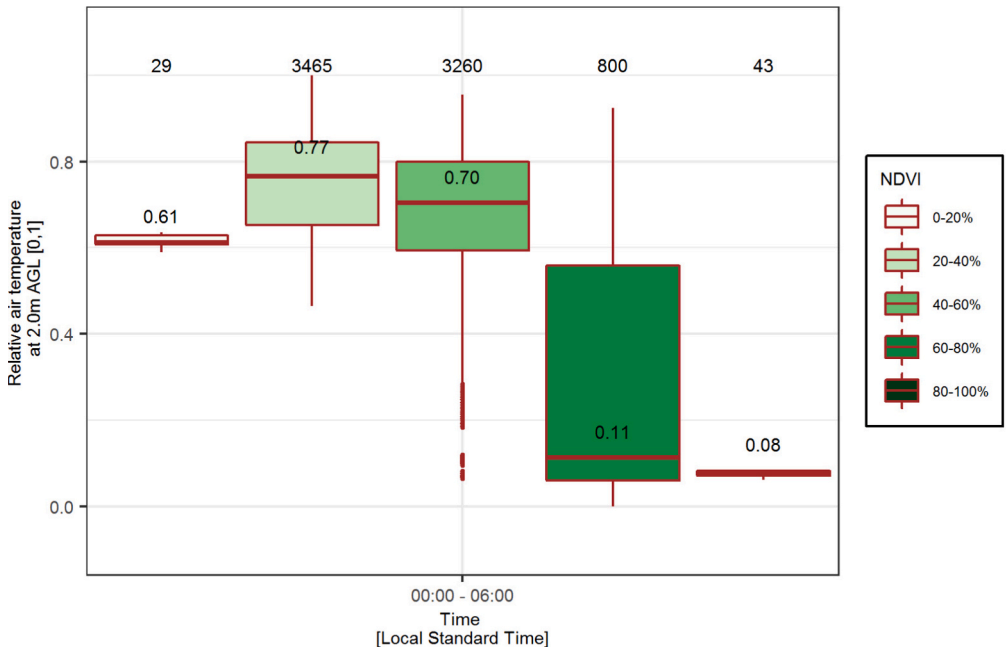

(a) Observed impact of NDVI on normalized and relative air temperature at 2.0 m AGL.

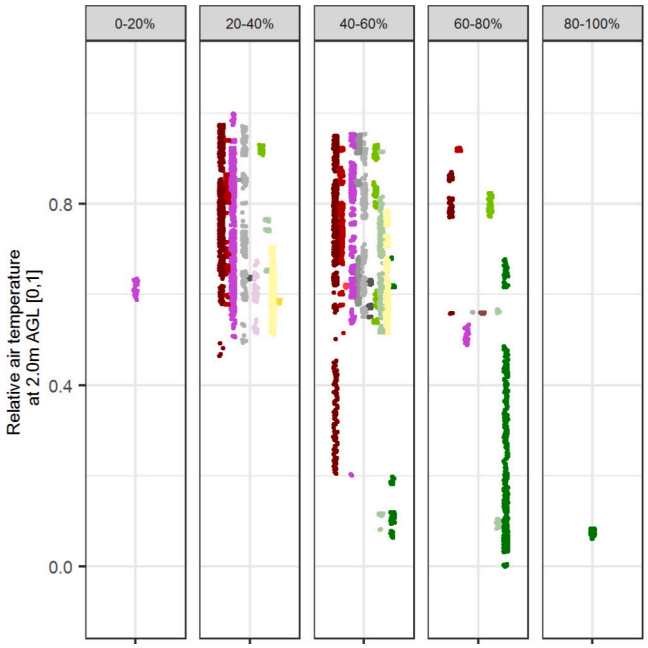

(b) Mapping of NDVI classes to Urban Atlas classification.

Fig. 16. Modification of relative and normalized air temperature at 2.0 m AGL by NDVI in the morning hours (22–4 UTC). NDVI is divided into groups with intervals of 20%, increasing from left to right. NDVI was calculated after (Ermida et al., 2020) within 100 m range of the route.

this is the case, it would be possible to assess all UHI intensities in absolute values. This is the reason, why the normalization procedure is most suitable to assess the spatial pattern of the UHI.

Besides the relative and normalized air temperature, one could also think about other relative and normalized meteorological variables (e.g., vapor pressure, wind speed, global radiation). However, it is necessary to find out how large the spatial variability of the individual variables is. If the variables have a large spatial variability, or if the range of values of the variable is very large (e.g., shaded vs. unshaded, calm vs. strong wind), then the mentioned method is not suitable, since small differences of the values are not recognizable.

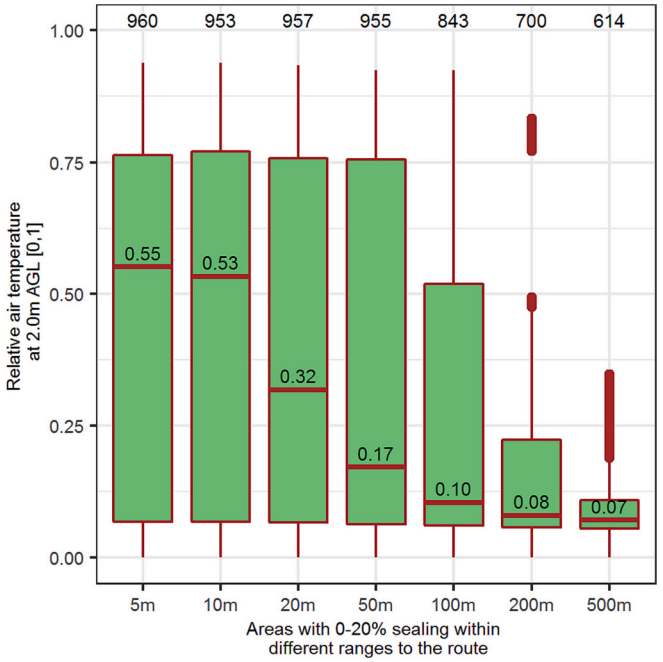

Fig. 17. Influence of the area size under consideration with NDVI between 60% -100%.

In order to assess generalized effects on humans, the calculation of relative and normalized thermal indices like perceived or physiologically equivalent temperature, could also be considered. But these indices require spatially-resolved wind speed along the measurement route which was not available, but could potentially be provided by numerical process-based models.

Other studies set the surveys in relation to the start- and end points of each measurement run (Romero Rodríguez et al., 2020b). Normalization was also applied for other cities (Szeged and Debrecen) to calculate correctly-weighted average values of the UHI, showing the concentric shape of the UHI effect observed by different measurements (Unger et al., 2010). In that case, the measurement runs were distributed throughout the year to obtain a comprehensive result. The individual measurement runs were mapped onto a discrete grid by averaging several measurement points within a 0.5 km × 0.5 km grid point. All grid points were then referenced to the rural reference cell according to the following equation:

$$\Delta T_a = T_{a,urban} - T_{a,rural} \tag{6}$$

It is not necessarily given that the rural cell also represents the minimum value, since the selection of rural and urban sites is not standardized.

In our study, each individual measurement run was normalized separately, so that the minimum and maximum values refer to the individual measurement run (Eq. 3), while (Unger et al., 2010) applied the normalization procedure on the discrete grid according to:

$$\Delta T_{norm} = \frac{T_{cell} - T_{rural}}{T_{cell(max)} - T_{rural}} \# \tag{7}$$

In addition to determining the outdoor conditions of human thermal comfort, indoor conditions are of great importance because people in the city spend much of their time at work indoors (Sulzer et al., 2022).

4.2. Accuracy of GNSS in cities

The positioning accuracy is limited due to shading and reflections of the GNSS signals in street canyons. (Merry and Bettinger, 2019) demonstrated that GPS accuracy of smartphones is in the range of 7 m to 13 m on average. (Abdi et al., 2014) showed that GPS accuracy in urban green space is within the range of 9 m to 12 m, and depends on the time of day and the season. Our observations fit to this range with a mean error of 9.2 m (Fig. 4).

The preparation of the specific positions posed a particular challenge, as the inaccuracies with respect to the road were nevertheless very large. In the future, an improved position determination in the city could be achieved by a Differential Global Positioning System (DGPS), by correction method Real Time Kinetics (RTK), or by the advanced Post Processed Kinematic (PPK) in combination with an Inertial Measurement Unit (IMU) on the measurement vehicle (Puente et al., 2013).

The inaccuracy is not only in the location of the measurement points, but also in the location of the administrative geodata (e.g., positions of street trees in urban tree cadasters, if provided by GPS and not georeferenced orthophotos).

We improved accuracy by error reduction in the preprocessing, using the background knowledge from really driving on the road

and introducing standardized measuring points. To our knowledge, such a procedure has not yet been applied for mobile measurement runs to determine the UHI. In addition to the positional inaccuracies of the measurement runs and the data of the administrative geodata, there are also inaccuracies in the space-borne, remotely-sensed datasets (e.g., NDVI has a spatial resolution of 20 m).

4.3. Spatial autocorrelation

Tobler's first law of geography is also valid in Karlsruhe: “everything is related to everything else, but near things are more related than distant things”. However, the spatial continuity of meteorological conditions depends on the time of day, as they are modified by different processes in the city. This is particularly evident from the variogram (Fig. 10), but also from the direct comparison between the individual time intervals of the measurement runs (Fig. 9 - Fig. 13). Fig. 6, Fig. 15, and Fig. 17 also make it clear that it is not only the closer neighborhood that is important in modifying the meteorological conditions, but also the urban structures that are located some distance away.

The large spatial auto-correlation at night can perhaps be attributed to limited mixing by convection and advection. The absence of shortwave radiation at night, especially Photosynthetically Active Radiation, suspends the tree-physiological processes controlled by radiation (e.g., transpiration and photosynthesis) (Jones, 2013; Monteith and Unsworth, 2013). Energy conversion at building surfaces is also limited, except for the emission of longwave radiation (Oke et al., 2017).

In contrast, thermal and radiation-based processes are intensified in the morning with increase in global radiation. Due to a large Sky View Factor, these processes start especially in open spaces in the city, because the upper hemisphere is only slightly obscured by buildings (Gangwisch et al., 2021). During the day, the coldest spots in the city are found in the *Hardtwald* (LCZ B) area as well as in the *Zoologischer Stadtgarten* (LCZ 6 and B), which could be related to intensified cooling by transpiration and shading. Unfortunately, we could not determine the tree-physiological processes (e.g., sap-flow, transpiration rates, stomatal conductance) during our measurements.

Furthermore, the spatial auto-correlation is lowest during the day. The variogram shows a large variance, which is possibly caused by the mixing of the atmosphere by convection and advection. Concurrently, this makes it very difficult to determine the thermal effects of microscale structures, since it can no longer be traced back to individual structures.

4.4. Spatial neighborhood analysis - links between atmospheric conditions, urban descriptors and buffer sizes

We use circular buffers to spatially quantify neighborhoods' influence. By doing so, we made the assumption that all urban structures in the neighborhood contribute equally to meteorological conditions. However, this assumption is not valid under conditions with higher wind speeds. According to the wind direction, the influence of urban structures would have to be weighted more heavily upwind, and weaker to none at all downwind. This could possibly be realized by eccentric buffers. In addition, the influence of nearby structures should be weighted more heavily than the influence of structures that are distant. However, during our measurements there was only very weak wind. Furthermore, observations with wind speeds $> 3.0\ m \cdot s^{-1}$ and $< 0.5\ m \cdot s^{-1}$ were filtered out. In principle, spatial neighborhood analysis can be applied to different spatial descriptors to describe the neighborhood. We focus on parameters describing vegetation and sealing; but other descriptors (e.g. building height, building density, etc.) are quite conceivable.

4.4.1. Links between atmospheric conditions and land-use classes

(Aksoy et al., 2022) demonstrated that Urban Atlas provides higher spatial resolution and improved accuracy compared to CORINE land cover. In contrast to CORINE land cover (one class for urban areas), Urban Atlas provides four distinguished classes for urban areas, and is therefore more suitable for urban microscale analyses of outdoor human thermal comfort. It was shown that urban structures have the greatest impact to increase relative and normalized air temperature at 2.0 m AGL (Fig. 16b). In particular, densely-populated areas, industrial areas (with flat roofs) and streets were the warmest. In contrast, natural areas (urban forests and parks) were the coldest among the study area. But Urban Atlas classes also show inner zonal variation of meteorological conditions in each class. In general, no statements can be made about land uses that do not occur along the route. For example, water areas hardly occur, and the city center of Karlsruhe is not topographically characterized, so that these results cannot be transferred to other cities with larger water areas or elevations.

4.4.2. The links between atmospheric conditions and urban vegetation was considered by the NDVI

We used NDVI because this vegetation index is available area-wide for all of Karlsruhe. However, NDVI has the disadvantage that it is not possible to distinguish between low- and high vegetation cover. Here, in the middle latitudes, there might be the possibility to calculate a summer and a winter NDVI to at least distinguish between deciduous and coniferous trees. In addition, there are now also approaches from the field of machine learning that allow the vegetation types to be determined from LiDAR-generated point clouds.

The most important variable that has an influence on transpirational cooling of urban trees is water availability in the root zone. Unfortunately, spatially-resolved data on water availability were not available to us. Thus, we also do not have information on the irrigation of urban vegetation.

The results showed that the size of the green cover has great influence on the cooling potential of the green space. Larger green areas should therefore be preferred.

However, these statements are only valid for the meteorological conditions under which the measurements were carried out, since the day of the year or seasonality also has a great influence due to different adaptation of the vegetation.

Our analysis also revealed that sealing in Karlsruhe is inversely related to the NDVI.

5. Conclusion

The relative and normalized air temperature is a suitable methodology to generalize from prevailing weather conditions in order to get a typified insight into the thermal response of an urban environment. Therefore, the relative and normalized air temperature allows for the detection of anomalies of meteorological conditions throughout urban environments. It does not matter at which time and at which location on earth the observations were recorded. But, it is very important that the observations were assessed under similar conditions (autochthonous day with low wind speed and clear sky conditions). With the help of the normalized air temperature, however, no statements can then be made about the effects of individual weather conditions.

The normalized air temperature is an additional tool for long-term, climate-adapted urban planning for a city like Karlsruhe. Thus, this information can be used for decision-making in setting up long-term measures (in urban planning and building construction) embedded in heat action plans. Furthermore, it is possible to transfer the methodology to different cities by design, and compare different patterns of urban heat islands.

The method could also be used in short-term climate adaptation as part of a specific and localized heat warning system. Here, the method offers the possibility to relate the spatially resolved risk of a heat wave (in terms of cool and hot areas in the city) to risk and protection factors.

The imposed spatial neighborhood analysis showed the effects of vegetation and sealing in relation to reference areas of different sizes. Both sealing and vegetation cover play a very important role in modifying the thermal pattern of the UHI. Adapted urban planning for the adaptation to global climate change must therefore consider both the unsealing of urban areas and the maintenance of the vegetation cover. The spatial neighborhood analysis requires a combination of remote sensing, observation and administrative data in order to get a comprehensive picture covering all information available on the three-dimensional structure of a city.

CRediT authorship contribution statement

Marcel Gangwisch: Conceptualization, Methodology, Software, Formal analysis, Investigation, Data curation, Writing – original draft, Writing – review & editing, Visualization. **Somidh Saha:** Conceptualization, Resources, Writing – review & editing, Supervision, Project administration, Funding acquisition. **Andreas Matzarakis:** Conceptualization, Resources, Writing – review & editing, Supervision, Project administration, Funding acquisition.

Declaration of Competing Interest

The authors declare that they have no known competing financial interests or personal relationships that could have appeared to influence the work reported in this paper.

Data availability

The authors do not have permission to share data.

Acknowledgement

We want to thank the German Aerospace Center (Das Deutsche Zentrum für Luft- und Raumfahrt e.V.) and the Federal Ministry of Education and Research of Germany (Das Bundesministerium für Bildung und Forschung - BMBF) for providing the financial support (GrüneLunge project - funding reference number 01LR1726C, https://www.projekt-gruenelunge.de/). The project is part of the *Zukunftsstadt* program (https://www.innovationsplattform-zukunftsstadt.de/, last access: 21 October 2020).

The authors would also like to thank the team of the Mobile Messeinheit (MME) in Potsdam for thoroughly carrying out the measurement runs.

Appendix A. Impact of degree of sealing and spatial range on relative and normalized air temperature at 2.0 M AGL

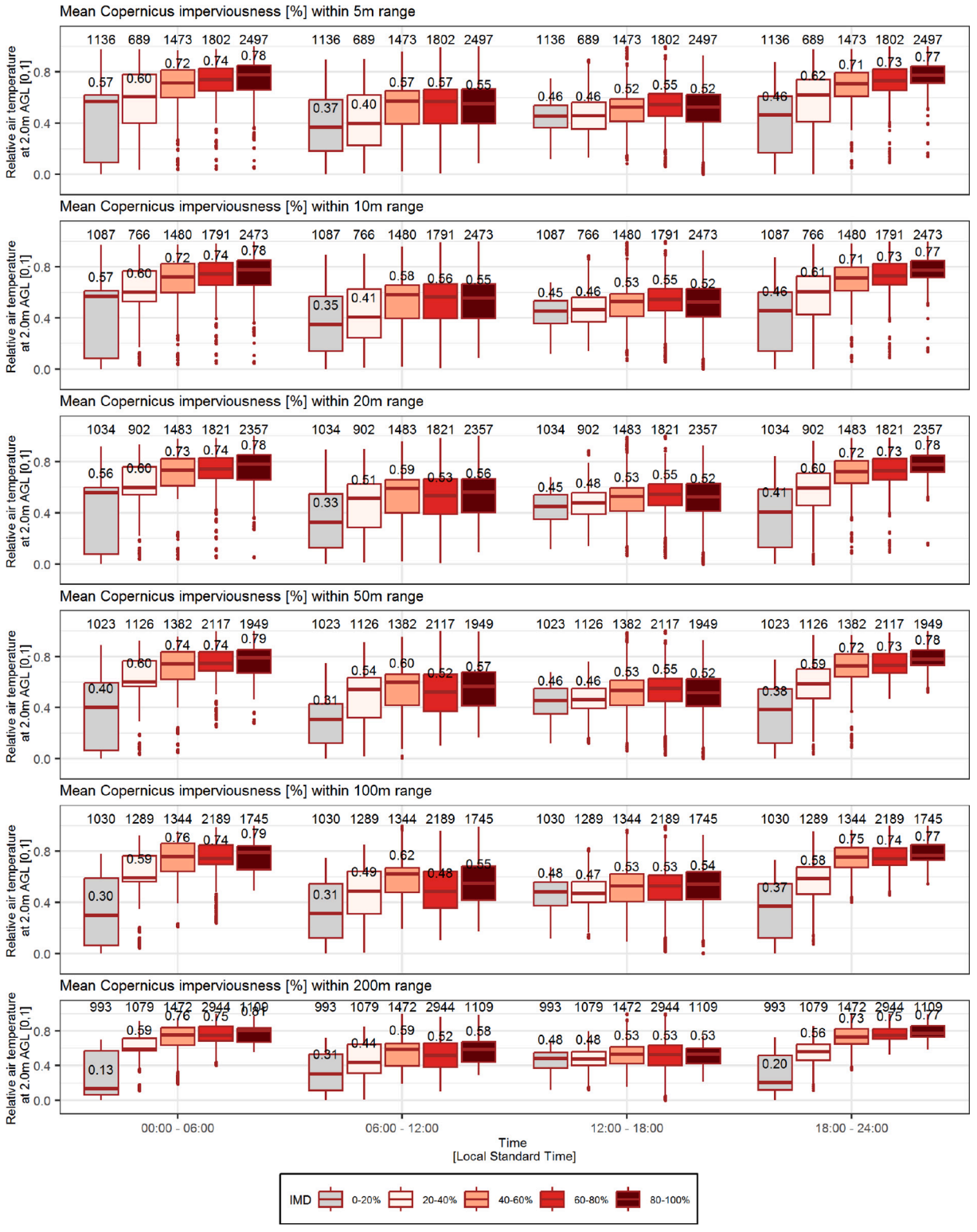

Appendix B. Impact of NDVI and spatial range on relative and normalized air temperature AT 2.0 M AGL

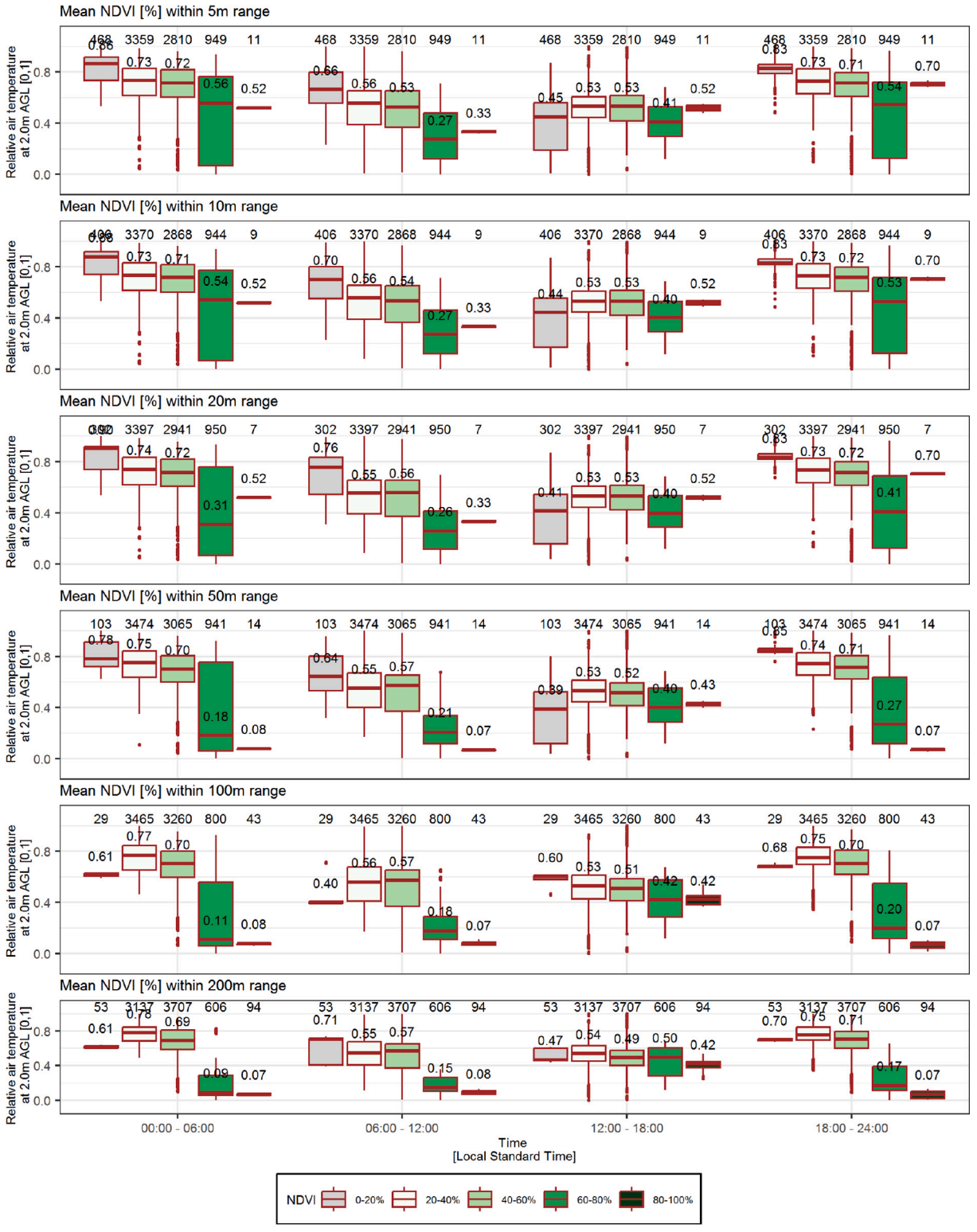
Mean NDVI [%] within 5m range
Mean NDVI [%] within 10m range
Mean NDVI [%] within 20m range
Mean NDVI [%] within 50m range
Mean NDVI [%] within 100m range
Mean NDVI [%] within 200m range
Relative air temperature at 2.0m AGL [0,1]
0.0
0.4
0.8
00:00 - 06:00
06:00 - 12:00
12:00 - 18:00
18:00 - 24:00
Time
[Local Standard Time]
NDVI
0-20%
20-40%
40-60%
60-80%
80-100%

References

Abdi, E., Mariv, H.S., Deljouei, A., Sohrabi, H., 2014. Accuracy and precision of consumer-grade GPS positioning in an urban green space environment. For. Sci. Technol. 10 (3), 141–147. https://doi.org/10.1080/21580103.2014.887041.

Aksoy, T., Dabanli, A., Cetin, M., Senyel Kurkcuoglu, M.A., Cengiz, A.E., Cabuk, S.N., Agacsapan, B., Cabuk, A., 2022. Evaluation of comparing urban area land use change with urban atlas and CORINE data. Environ. Sci. Pollut. Res. 29 (19), 28995–29015. https://doi.org/10.1007/s11356-021-17766-y.

Arnfield, A.J., 2003. Two decades of urban climate research: a review of turbulence, exchanges of energy and water, and the urban heat island. Int. J. Climatol. 23 (1), 1–26. https://doi.org/10.1002/joc.859.

ASHRAE, 2017. 2017 ASHRAE Handbook: Fundamentals.

Chandler, T.J., 1962. Temperature and humidity traverses across London. Weather 17 (7), 235–242. https://doi.org/10.1002/j.1477-8696.1962.tb05125.x.

Charalampopoulos, I., 2020. The R language as a tool for biometeorological research. Atmosphere 11 (7), 682. https://doi.org/10.3390/atmos11070682.

Conrad, O., Bechtel, B., Bock, M., Dietrich, H., Fischer, E., Gerlitz, L., Wehberg, J., Wichmann, V., Böhner, J., 2015. System for automated geoscientific analyses (SAGA) v. 2.1.4. Geosci. Model Dev. 8 (7), 1991–2007. https://doi.org/10.5194/gmd-8-1991-2015.

D'Acci, L. (Ed.), 2019. The Mathematics of Urban Morphology. Springer International Publishing. https://doi.org/10.1007/978-3-030-12381-9.

Demuzere, M., Bechtel, B., Middel, A., Mills, G., 2019. Mapping Europe into local climate zones. PLoS One 14 (4), e0214474. https://doi.org/10.1371/journal.pone.0214474.

Dobrovolný, P., Krahula, L., 2015. The spatial variability of air temperature and nocturnal urban heat island intensity in the city of Brno, Czech Republic. Moravian Geograph. Rep. 23 (3), 8–16. https://doi.org/10.1515/mgr-2015-0013.

Ermida, S.L., Soares, P., Mantas, V., Göttsche, F.-M., Trigo, I.F., 2020. Google earth engine open-source code for land surface temperature estimation from the Landsat series. Remote Sens. 12 (9), 1471. https://doi.org/10.3390/rs12091471.

European Union, 2018. Copernicus Land Monitoring Service 2018. European Environment Agency (EEA).

van den Bosch, C., 2017. In: Ferrini, F., Fini, A. (Eds.), Routledge Handbook of Urban Forestry. Routledge/Taylor & Francis.

Gangwisch, M., Fröhlich, D., Christen, A., Matzarakis, A., 2021. Geometrical assessment of sunlit and shaded area of urban trees based on aligned orthographic views. Atmosphere 12 (8), 968. https://doi.org/10.3390/atmos12080968.

Gehl, J., 2010. Cities for People. Island Press.

Hackenbruch, J., 2018. Anpassungsrelevante Klimaänderungen für städtische Baustrukturen und Wohnquartiere. KIT Scientific Publishing.

Höppe, P., 1999. The physiological equivalent temperature—a universal index for the biometeorological assessment of the thermal environment. Int. J. Biometeorol. 43 (2), 71–75. https://doi.org/10.1007/s004840050118.

Jendritzky, G., de Dear, R., Havenith, G., 2012. UTCI–why another thermal index? Int. J. Biometeorol. 56 (3), 421–428. https://doi.org/10.1007/s00484-011-0513-7.

Jones, H.G., 2013. Plants and Microclimate: A Quantitative Approach to Environmental Plant Physiology, 3rd ed. Cambridge University Press. https://doi.org/10.1017/CBO9780511845727.

Karlsruhe, Stadt, 2021. Statistisches Jahrbuch, p. 2021. https://web6.karlsruhe.de/Stadtentwicklung/statistik/pdf/2021/2021-jahrbuch.pdf.

Keil, M., Kiefl, R., Strunz, G., 2005. CORINE Land Cover 2000—European-Wide Harmonised Update of Land Use Data for Germany. DLR. /z-wcorg/.

Ketterer, C., Matzarakis, A., 2015. Comparison of different methods for the assessment of the urban heat island in Stuttgart, Germany. Int. J. Biometeorol. 59 (9), 1299–1309. https://doi.org/10.1007/s00484-014-0940-3.

Kotharkar, R., Surawar, M., 2016. Land use, land cover, and population density impact on the formation of canopy urban Heat Islands through traverse survey in the Nagpur urban area, India. J. Urban Plann. Develop. 142 (1), 04015003. https://doi.org/10.1061/(ASCE)UP.1943-5444.0000277.

Leconte, F., Bouyer, J., Claverie, R., Pétrissans, M., 2015. Using local climate zone scheme for UHI assessment: evaluation of the method using mobile measurements. Build. Environ. 83, 39–49. https://doi.org/10.1016/j.buildenv.2014.05.005.

Lehnert, M., Geletič, J., Husák, J., Vysoudil, M., 2015. Urban field classification by "local climate zones" in a medium-sized central European city: the case of Olomouc (Czech Republic). Theor. Appl. Climatol. 122 (3–4), 531–541. https://doi.org/10.1007/s00704-014-1309-6.

Lehnert, M., Savić, S., Milošević, D., Dunjić, J., Geletič, J., 2021. Mapping local climate zones and their applications in European urban environments: a systematic literature review and future development trends. ISPRS Int. J. Geo Inf. 10 (4), 260. https://doi.org/10.3390/ijgi10040260.

Liu, L., Lin, Y., Liu, J., Wang, L., Wang, D., Shui, T., Chen, X., Wu, Q., 2017. Analysis of local-scale urban heat island characteristics using an integrated method of mobile measurement and GIS-based spatial interpolation. Build. Environ. 117, 191–207. https://doi.org/10.1016/j.buildenv.2017.03.013.

Longley, P. (Ed.), 2005. Geographical Information Systems: Principles, Techniques, Management, and Applications, 2nd ed., abridged. John Wiley & Sons.

Masson, V., Heldens, W., Bocher, E., Bonhomme, M., Bucher, B., Burmeister, C., de Munck, C., Esch, T., Hidalgo, J., Kanani-Sühring, F., Kwok, Y.-T., Lemonsu, A., Lévy, J.-P., Maronga, B., Pavlik, D., Petit, G., See, L., Schoetter, R., Tornay, N., Zeidler, J., 2020a. City-descriptive input data for urban climate models: model requirements, data sources and challenges. Urban Clim. 31, 100536 https://doi.org/10.1016/j.uclim.2019.100536.

Masson, V., Lemonsu, A., Hidalgo, J., Voogt, J., 2020b. Urban climates and climate change. Annu. Rev. Environ. Resour. 45 (1), 411–444. https://doi.org/10.1146/annurev-environ-012320-083623.

Matzarakis, A., 2020. A note on the assessment of the effect of atmospheric factors and components on humans. Atmosphere 11 (12), 1283. https://doi.org/10.3390/atmos11121283.

Matzarakis, A., Mayer, H., Iziomon, M.G., 1999. Applications of a universal thermal index: physiological equivalent temperature. Int. J. Biometeorol. 43 (2), 76–84. https://doi.org/10.1007/s004840050119.

Merry, K., Bettinger, P., 2019. Smartphone GPS accuracy study in an urban environment. PLoS One 14 (7), e0219890. https://doi.org/10.1371/journal.pone.0219890.

Monteith, J.L., Unsworth, M.H., 2013. Principles of Environmental Physics: Plants, Animals, and the Atmosphere, 4. ed. Elsevier/Acad. Press.

Morakinyo, T.E., Ouyang, W., Lau, K.K.-L., Ren, C., Ng, E., 2020. Right tree, right place (urban canyon): tree species selection approach for optimum urban heat mitigation - development and evaluation. Sci. Total Environ. 719, 137461 https://doi.org/10.1016/j.scitotenv.2020.137461.

Nowak, D.J., Greenfield, E.J., 2020. The increase of impervious cover and decrease of tree cover within urban areas globally (2012–2017). Urban For. Urban Green. 49, 126638 https://doi.org/10.1016/j.ufug.2020.126638.

Oke, T.R., 2004. Initial Guidance to Obtain Representative Meteorological Observations at Urban Sites.

Oke, T.R., Mills, G., Christen, A., Voogt, J.A., 2017. Urban Climates. Cambridge University Press. https://doi.org/10.1017/9781139016476.

Open Source Geospatial Foundation, 2018. QGIS Geographic Information System. http://qgis.osgeo.org.

Parsons, K.C., 2014. Human Thermal Environments: The Effects of Hot, Moderate, and Cold Environments on Human Health, Comfort, and Performance, 3. ed. CRC Press/Taylor & Francis.

Puente, I., González-Jorge, H., Martínez-Sánchez, J., Arias, P., 2013. Review of mobile mapping and surveying technologies. Measurement 46 (7), 2127–2145. https://doi.org/10.1016/j.measurement.2013.03.006.

R Core Team, 2019. *R: A Language and Environment for Statistical Computing* [Manual]. https://www.R-project.org/.

Rahman, M.A., Moser, A., Rötzer, T., Pauleit, S., 2017. Microclimatic differences and their influence on transpirational cooling of Tilia cordata in two contrasting street canyons in Munich, Germany. Agric. For. Meteorol. 232, 443–456. https://doi.org/10.1016/j.agrformet.2016.10.006.

Rahman, M.A., Stratopoulos, L.M.F., Moser-Reischl, A., Zölch, T., Häberle, K.-H., Rötzer, T., Pretzsch, H., Pauleit, S., 2020. Traits of trees for cooling urban heat islands: a meta-analysis. Build. Environ. 170, 106606 https://doi.org/10.1016/j.buildenv.2019.106606.

Revi, A., Satterthwaite, D.E., Aragón-Durand, F., Corfee-Morlot, J., Kiunsi, R.B.R., Pelling, M., Roberts, D.C., Solecki, W., 2014. Urban areas. In: Field, C.B., Barros, V. R., Dokken, D.J., Mach, K.J., Mastrandrea, M.D., Bilir, T.E., Chatterjee, M., Ebi, K.L., Estrada, Y.O., Genova, R.C., Girma, B., Kissel, E.S., Levy, A.N., MacCracken, S., Mastrandrea, P.R., White, L.L. (Eds.), Climate Change 2014: Impacts, Adaptation, and Vulnerability. Part A: Global and Sectoral Aspects. Contribution of Working Group II to the Fifth Assessment Report of the Intergovernmental Panel of Climate Change. Cambridge University Press, pp. 535–612.

Romero Rodríguez, L., Sánchez Ramos, J., Sánchez de la Flor, F.J., Álvarez Domínguez, S., 2020a. Analyzing the urban heat island: comprehensive methodology for data gathering and optimal design of mobile transects. Sustain. Cities Soc. 55, 102027 https://doi.org/10.1016/j.scs.2020.102027.
Romero Rodríguez, L., Sánchez Ramos, J., Sánchez de la Flor, F.J., Álvarez Domínguez, S., 2020b. Analyzing the urban heat island: comprehensive methodology for data gathering and optimal design of mobile transects. Sustain. Cities Soc. 55, 102027 https://doi.org/10.1016/j.scs.2020.102027.
Rubel, F., Kottek, M., 2010. Observed and projected climate shifts 1901-2100 depicted by world maps of the Köppen-Geiger climate classification. Meteorol. Z. 19 (2), 135–141. https://doi.org/10.1127/0941-2948/2010/0430.
Saaroni, H., Ben-Dor, E., Bitan, A., Potchter, O., 2000. Spatial distribution and microscale characteristics of the urban heat island in Tel-Aviv, Israel. Landsc. Urban Plan. 48 (1–2), 1–18. https://doi.org/10.1016/S0169-2046(99)00075-4.
Santamouris, M., 2015. Analyzing the heat island magnitude and characteristics in one hundred Asian and Australian cities and regions. Sci. Total Environ. 512–513, 582–598. https://doi.org/10.1016/j.scitotenv.2015.01.060.
Santamouris, M., 2020. Recent progress on urban overheating and heat island research. Integrated assessment of the energy, environmental, vulnerability and health impact. Synergies with the global climate change. Energy Build. 207, 109482 https://doi.org/10.1016/j.enbuild.2019.109482.
Shandas, V., Voelkel, J., Williams, J., Hoffman, J., 2019. Integrating satellite and ground measurements for predicting locations of extreme urban heat. Climate 7 (1), 5. https://doi.org/10.3390/cli7010005.
Sobrino, J.A., Oltra-Carrió, R., Sòria, G., Bianchi, R., Paganini, M., 2012. Impact of spatial resolution and satellite overpass time on evaluation of the surface urban heat island effects. Remote Sens. Environ. 117, 50–56. https://doi.org/10.1016/j.rse.2011.04.042.
Soltani, A., Sharifi, E., 2017. Daily variation of urban heat island effect and its correlations to urban greenery: a case study of Adelaide. Front. Architect. Res. 6 (4), 529–538. https://doi.org/10.1016/j.foar.2017.08.001.
Staiger, H., Laschewski, G., Matzarakis, A., 2019. Selection of appropriate thermal indices for applications in human biometeorological studies. Atmosphere 10 (1), 18. https://doi.org/10.3390/atmos10010018.
Stewart, I.D., 2011. Redefining the Urban Heat Island. https://doi.org/10.14288/1.0072360.
Stewart, I.D., Oke, T.R., 2012. Local climate zones for urban temperature studies. Bull. Am. Meteorol. Soc. 93 (12), 1879–1900. https://doi.org/10.1175/BAMS-D-11-00019.1.
Sulzer, M., Christen, A., Matzarakis, A., 2022. A low-cost sensor network for real-time thermal stress monitoring and communication in occupational contexts. Sensors 22 (5), 1828. https://doi.org/10.3390/s22051828.
Unger, J., Sümeghy, Z., Szegedi, S., Kiss, A., Géczi, R., 2010. Comparison and generalisation of spatial patterns of the urban heat island based on normalized values. Phys. Chem. Earth, Parts A/B/C 35 (1–2), 107–114. https://doi.org/10.1016/j.pce.2010.03.001.
VDI, 2021. VDI 3787 Blatt 2—Umweltmeteorologie—Methoden zur human-biometeorologischen Bewertung der thermischen Komponente des Klimas. https://www.vdi.de/richtlinien/details/vdi-3787-blatt-2-umweltmeteorologie-methoden-zur-human-biometeorologischen-bewertung-der-thermischen-komponente-des-klimas.
Voelkel, J., Shandas, V., 2017. Towards systematic prediction of urban Heat Islands: grounding measurements, assessing modeling techniques. Climate 5 (2), 41. https://doi.org/10.3390/cli5020041.
Voogt, J.A., Oke, T.R., 1998. Effects of urban surface geometry on remotely-sensed surface temperature. Int. J. Remote Sens. 19 (5), 895–920. https://doi.org/10.1080/014311698215784.
Voogt, J.A., Oke, T.R., 2003. Thermal remote sensing of urban climates. Remote Sens. Environ. 86 (3), 370–384. https://doi.org/10.1016/S0034-4257(03)00079-8.
Wang, X., Dallimer, M., Scott, C.E., Shi, W., Gao, J., 2021. Tree species richness and diversity predicts the magnitude of urban heat island mitigation effects of greenspaces. Sci. Total Environ. 770, 145211 https://doi.org/10.1016/j.scitotenv.2021.145211.
Węziak-Białowolska, D., 2016. Quality of life in cities – empirical evidence in comparative European perspective. Cities 58, 87–96. https://doi.org/10.1016/j.cities.2016.05.016.
Yutzler, J., 2021. OGC® GeoPackage Encoding Standard—with Corrigendum, Version 1.3.1. https://www.geopackage.org/spec131/.